Sequential MD-QM Approach to Compute Chemical Properties of Amorphous Silica-Based Catalysts

Rubirigi, Charles; Champagne, Benoît; Aprile, Carmela

Published in:
Advanced Theory and Simulation

DOI:
10.1002/adts.202501609

Publication date:
2026

Document Version
Peer reviewed version

Sequential MD-QM Approach to Compute Chemical Properties of Amorphous Silica-Based Catalysts: Brønsted Aluminosilicate Acids as Case Study

*Charles Rubirigi Carmela Aprile Benoît Champagne**

Charles Rubirigi, Prof. Dr. Benoît Champagne
Department of Chemistry, Theoretical Chemistry Lab, Unit of Theoretical and Structural Physical Chemistry, Namur Institute of Structured Matter (NISM), University of Namur 5000 Namur, Belgium
Email Address: benoit.champagne@unamur.be
Prof. Dr. Carmela Aprile
Department of Chemistry, Applied Materials Chemistry Lab, Unit of Nanomaterials Chemistry, Namur Institute of Structured Matter (NISM), University of Namur 5000 Namur, Belgium

Keywords: *MD-then-QM protocol, amorphous, aluminosilicates, deprotonation energy, NMR chemical shift*

Amorphous silica-based materials are often used as support for catalysis experiments. The insertion of heteroelements (i.e., neither a silicon nor an oxygen atom) leads to the formation of Brønsted or Lewis acid sites. Despite their widespread use, the characterization of their acidic properties and the correlation with structural features remain challenging. In this context, computing chemical properties with quantum chemical methods can bring insights into such materials, while the large size of these systems implies the use of models to control the computational effort. This work aims to present a general procedure for calculating chemical properties of amorphous silica-based catalysts. The amorphous network is generated using classical molecular dynamics via a thermal treatment called melt-and-quench. Particular attention is devoted to the catalyst shape and the silanol coverage. The quality of the final amorphous network is assessed through the characterization of the geometrical structures involving primitive ring analysis. DFT calculations are then performed on hemispheres extracted from the amorphous silica frameworks to model aluminosilicate Brønsted acid sites. The impact of cluster size on the prediction of chemical properties is illustrated by calculations of deprotonation energies, chemical shifts, and vibrational frequencies. The influence of the exchange-correlation (XC) functional on those quantities is also discussed.

1 Introduction

Catalysis is a central process in chemistry. It allows performing reactions under milder temperature and pressure conditions by lowering the activation energy.[1] The use of heterogeneous catalysts facilitates their separation from the reactive mixture. Among them, acid catalysts play a key role in many industrial reactions. In addition to their separability from the reaction mixture, solid acids are generally reusable and less hazardous than their homogeneous counterparts (*e.g.* HF, H_2SO_4).[2] However, due to their weak acidic character their use as acid catalysts requires a suitable modification of the surface and/or framework features.[3] Acid sites are generated by replacing one silicon atom with another element having similar physical properties.[4] A wide range of trivalent or tetravalent heteroatoms has been isomorphously incorporated in zeolites (crystalline silica structures) such as Be^{2+}, Zn^{2+}, B^{3+}, Al^{3+}, Ga^{3+}, Fe^{3+}, Ge^{4+}, Ti^{4+}, and Sn^{4+}.[5] The heteroelement nature determines both the ratio between the acid types and their strengths.[6] For instance, atoms from the boron group (B, Al, Ga, and In) can act as Brønsted and Lewis

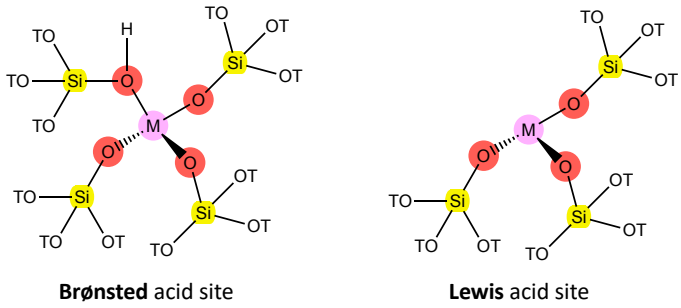

Figure 1: Models of Brønsted and Lewis acid sites generated by the insertion of an atom (M) from the boron group inside a silica framework.

acid sites depending on their surrounding within the framework (Figure 1).[7–10] The isomorphic substitution is guided by the energy consumed to distort the structure and the entropy gained by lowering the global order.[4] Silica-based catalysts can adopt an amorphous structure. The absence of a well-defined crystalline arrangement makes those materials more easily tunable but also more complex to characterize.

Although these amorphous materials are widely used, there is still a lack of understanding of their acidic properties.[11] Several experimental methods have been developed to study (amorphous and crystalline) heterogeneous catalysts, as well as to quantify their acidity character.[12] However, they are not able to give a complete picture of what is happening at the molecular scale. This is especially the case for phenomena occurring on the surface like catalytic reactions. Computational chemistry tools can help to fill this gap, by solving the electronic structure of atoms involved in the catalytic process.[13–15] However, unlike molecular catalysts, solid catalysts are often too large for direct quantum chemistry calculations on the whole structure. They must, therefore, be represented by a model, and these models must reproduce the properties of the studied material while circumventing computational power limitations.[16] In addition to being essential, building the most realistic model is a challenge in the context of catalysis using amorphous materials.

Two main schemes are usually employed to model solid-state catalysts: the periodic and the cluster approaches.[17–19] In the former case, a representative piece of the system is repeated in the 3 dimensions of the space and the electronic structure and properties are evaluated using crystalline orbitals and Periodic Boundary Conditions (PBC). In the latter case, a small part of the molecular structure is extracted, and calculations are performed on isolated species. Unlike in the cluster approach, the solid state character (and its long-range interactions) is retained in PBC calculations. On the other hand, the cluster approach enables to work on smaller systems, thus reducing computational costs. It also allows performing reference calculations with high-level wavefunction methods while it requires assessing the convergence of the results as a function of the cluster size.[20] Furthermore, the most widely used Quantum Mechanics (QM) methods in catalysis are derived from Density Functional Theory (DFT), and the use of hybrid exchange-correlation (XC) functionals is discouraged by their high computational costs within PBC.[19] For those reasons, this work presents a multistep procedure spanning from the production of an amorphous silica box to DFT calculations on Brønsted aluminosilicate clusters.

This work starts with the production of an amorphous silica framework and the steps involved in shaping a realistic catalyst (creation of a hydrated surface and modeling of a porous structure). Next, the

extraction of a Brønsted acid site cluster from the amorphous silica and the protocol to calculate the properties of the active site are presented. The work continues with an in-depth analysis of the structural properties of the amorphous system. Finally, the influence of cluster size and the impact of the XC functional on selected properties, chemical shifts (δ) and deprotonation energies (DPE), are discussed.

2 MD-then-QM computational approach

The large amount of atoms constituting silica-based catalysts implies the use of models to limit the computational resources. The cluster approach, chosen here, requires the production of an amorphous silica structure by Molecular Dynamics (MD). Quantum chemistry calculations are then performed on several clusters extracted from the generated structures, estimating a statistical distribution of the targeted properties. Brønsted aluminosilicate clusters are modeled to illustrate this sequential MD-then-QM procedure. This protocol is intended to be general and therefore, provided minor adaptation, applicable to systems carrying different heteroelements or modeling Lewis acid sites.

2.1 The MD-based melt-and-quench method

Due to its amorphous nature, the catalyst structure cannot be extracted from databases. As mentioned above, it must be represented by a model. There exist many schemes to model amorphous silica surfaces. One of them consists of using small silica structures, such as β-cristobalite surface (one of the crystalline forms of silica) or silsesquioxane (a small silica cage).[21,22] However, those models lack long-range disorder, which is characteristic of amorphous materials. Nowadays, the main technique for creating an amorphous silica framework is a procedure called melt-and-quench (Figure 2). This is a thermal treatment where a SiO_2 crystal is heated at a high temperature to produce a liquid, then cooled down at a certain rate to generate a disordered solid.[23]

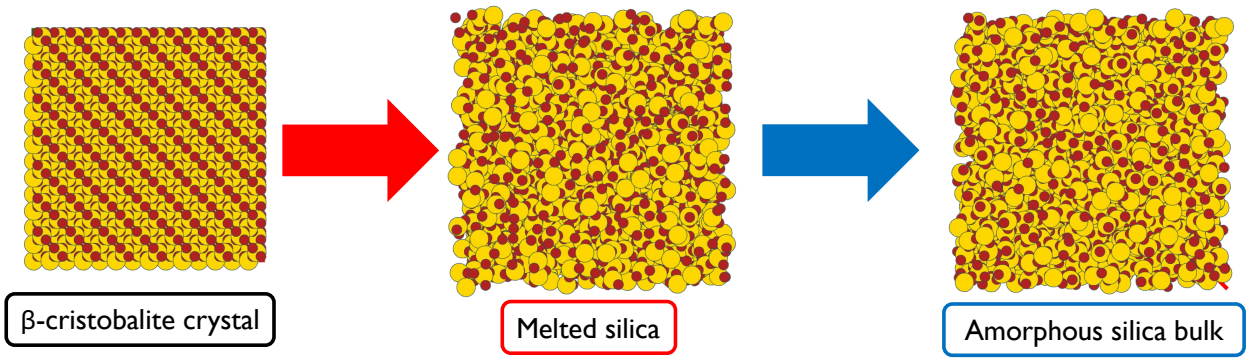

Figure 2: Melt-and-quench procedure for the production of an amorphous silica framework from a β-cristobalite supercell. The crystal is heated at 5000 K then cooled down to 300 K at a cooling rate of 5 K ps^{-1} to yield a disordered solid. Color code: Si in red and O in yellow.

It was adopted here by using β-cristobalite as starting structure, which constitutes the usual procedure.[24] This process is performed with MD, where the Newton equations of motion are solved through time. The interactions between atoms are described via an empirical equation, called a Force Field (FF). It allows investigating larger systems than with QM methods.[25] The Beest-Kramer-van Santen (BKS)[26] FF was selected because it has been shown to yield realistic amorphous silica structures.[27] (Equation (1))

$$V_{BKS}(r_{ij}) = A_{ij}\exp(-B_{ij}r_{ij}) - \frac{C_{ij}}{r_{ij}^6} + \frac{q_i q_j}{4\pi\epsilon_0 r_{ij}} \quad (1)$$

where r_{ij} is the distance between atoms i and j, q_i is the charge of the atom i, ϵ_0 is the vacuum permittivity, A_{ij} and B_{ij} are the parameters of the Buckingham repulsive term, and C_{ij} is the parameter of the attractive term. The parameters are presented in Table 1.

Table 1: BKS potential parameters.[26]

Atom 1	Atom 2	A_{ij} [kcal mol^{-1}]	B_{ij} [Å^{-1}]	C_{ij} [kcal Å^6 mol^{-1}]
O	O	32025.86	2.76	4036
O	Si	415176.39	4.87	3079
Si	Si	0	0	0

Nevertheless, at short distances, the BKS potential is replaced by a Lennard-Jones (LJ) potential to avoid unphysical situations (Equations (2-4)). The switch is made at 1.2 Å and 1.6 Å for the Si-O and O-O interactions, respectively.[28]

$$V_{LJ}(r_{ij}) = 4\epsilon_{ij}\left[\left(\frac{\sigma_{ij}}{r_{ij}}\right)^{12} - \left(\frac{\sigma_{ij}}{r_{ij}}\right)^{6}\right] \quad (2)$$

$$\sigma_{ij} = \frac{\sigma_i + \sigma_j}{2} \quad (3)$$

$$\epsilon_{ij} = \sqrt{\epsilon_i \epsilon_j} \quad (4)$$

where σ_i and ϵ_i are the LJ parameters for atom i and r_{ij} is the distance between atoms i and j. The parameters and charges for each atom are presented in Table 2.

Table 2: LJ and electrostatic parameters used in the BKS and CLAYFF potentials.[29,30]

	BKS			CLAYFF		
	ϵ_i [kcal mol^{-1}]	σ_i[Å]	q_i [e]	ϵ_i [kcal mol^{-1}]	σ_i[Å]	q_i [e]
O	-0.15	1.75	2.1	-0.1554	1.7766	-1.050
Si	-0.3	2.1475	-1.2	-1.84x10^{-6}	1.8532	2.1
H				0	0	0.425
OSI				-0.1554	1.7766	-0.950

The melt-and-quench procedure was enacted with the NAMD2.14 software[31] within PBC. A β-cristobalite unit cell (a=b=c=7.12 Å, α=β=γ=90°) is taken as the starting structure. The procedure was applied on a 7x7x7 cubic supercell containing 8232 atoms with an edge length of 49.84 Å. During the melting step, the crystal is heated at 5000 K for 1 ns at 1 atm. This process is carried out in the canonical ensemble (NPT). The temperature is controlled by a Langevin thermostat with a damping coefficient of 1 ps^{-1}. The pressure was set by a Langevin piston with a period of 100 fs and a decay of 50 fs. The cooling procedure takes place directly after the melting process. A cooling rate of 5 K ps^{-1} was applied for lowering the temperature by 100 K every 20 ps at 1 atm. The electrostatic interactions are evaluated using the Particle mesh Ewald (PME) method.

2.2 Generation of a surface

2.2.1 Surface creation and saturation of dangling bonds

As mentioned in the introduction, catalytic processes occur at the interface between the catalyst surface and the reactants. One simple way to generate a surface is to create a slab from the simulation box. This is done by increasing one of the edges of the simulation box. As a consequence, the newly created surface contains a large proportion of undercoordinated atoms. These anomalies are corrected by deleting atoms with lower valency and by saturating the surface oxygen atoms that are only bonded to one silicon atom. Saturating an oxygen atom consists of attaching one hydrogen atom to form a silanol function (the corresponding silanol oxygen is denoted OSI). Geske et al.[24] and Williams et al.[32] proposed an algorithm to saturate a silica surface (Figure 3). It first computes the number of neighbors each atom possesses (two atoms of the same kind cannot be bonded). A silicon atom i is considered bonded to an oxygen atom j, if i is one of the two nearest neighbors of j and j is one of the four nearest neighbors of i (with a maximum bond length of 2.1 Å). Knowing this information, the procedure adopted works as follows:

1. All silicon atoms bonded to less than 4 oxygen atoms are deleted.
2. All non-bonded oxygen atoms are removed.
3. Hydrogen atoms are attached to oxygen atoms that are only bonded to one silicon atom, at a distance of 1 Å, to form a silanol function.

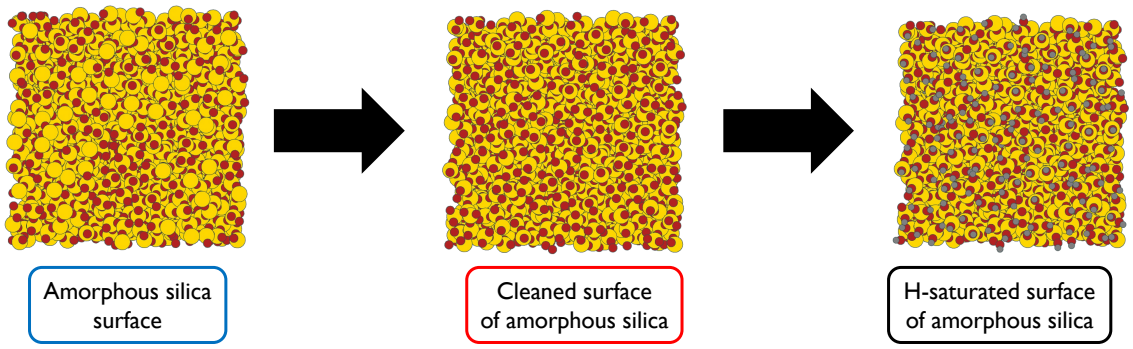

Figure 3: Steps to generate a realistic silica surface from an amorphous silica slab. The undercoordinated atoms are first removed then hydrogen atoms are added on single-bonded oxygen atoms. Color code: Si in red, O in yellow, and H in grey.

In practice, a slab was created from the amorphous silica box by increasing the edge of the simulation box in the z-direction by 20 Å. 390 hydrogen atoms have been added during the procedure, yielding a silica slab with 8409 atoms. The saturation algorithm only relies on geometric parameters, therefore, some of the newly created hydroxyl groups are in strained positions. An additional MD simulation is therefore necessary to avoid unphysical situations. Since the BKS FF does not contain any parameter for hydrogen atoms, the surface relaxation was performed with the CLAYFF potential.[30] It is commonly used to simulate zeolites and clays. It contains additional parameters for the hydrogen atom. While the BKS FF does not possess explicit bonding terms, CLAYFF describes bonds and angles at the surface with harmonic potentials (Equations (5-7)).

$$V_{CLAYFF}(r_{ij}) = V_{Coul} + V_{LJ} + V_{bond} + V_{angle} \quad (5)$$

$$V_{bond}(r_{ij}) = k_r(r_{ij} - r_{ij,0})^2 \quad (6)$$

$$V_{angle}(\theta_{ijk}) = k_\theta(\theta_{ijk} - \theta_{ijk,0})^2 \quad (7)$$

where V_{Coul} (last term of Equation (1)), V_{LJ} (Equation (2)), $V_{bonding}$, and V_{angle} are the Coulomb, LJ, bond and angle potentials, r_{ij} is the distance between atoms i and j, $r_{ij,0}$ is the equilibrium bond distance, k_r is the spring constant, θ_{ijk} is the angle between atoms i, j, and k, $\theta_{ijk,0}$ is the equilibrium angle and, k_θ is the angle force constant. The parameters are presented in Table 3. Although CLAYFF has not been designed to simulate amorphous silica frameworks, it is adequate to relax the surface. The relaxation was performed in the NPT ensemble at 300 K and 1 atm for 100 ps. The Langevin thermostat and barostat parameters from the melt-and-quench procedure were kept unchanged.

Table 3: Harmonic bonding and angle parameters for the CLAYFF potential.[30]

Atom 1	Atom 2	k_r [kcal mol^{-1} Å^{-2}]	$r_{ij,0}$[Å]	
OSI	H	554.13	1.00	
Atom 1	Atom 2	Atom 3	k_θ [kcal mol^{-1} °$^{-2}$]	$\theta_{ijk,0}$ [°]
Si	OSI	H	30	109.47

2.2.2 Dehydroxylation of the surfaces

Slabs are described by their silanol concentration (α_{OH}), which measures the amount of hydrogen atoms on the surface. 390 hydrogen atoms distributed on the two surfaces of dimensions 50.00 Å x 49.83 Å correspond to an α_{OH} of 7.9 OH nm^{-2}. Similar concentrations have been observed on hydrated silica materials.[33] However, silica-based catalysts usually undergo thermal treatment, resulting in lower α_{OH} (4-6 OH nm^{-2}). Several methods exist to produce silica surfaces with more realistic α_{OH}.[18] Tielens et al.[34] started from an unsaturated amorphous silica surface and simulated its hydration by water molecules with Ab Initio Molecular Dynamics (AIMD). Ewing et al.[35] started from a hydrated amorphous silica surface and reduced the α_{OH} iteratively. They computed the Gibbs free energy of dehydroxylation at the DFT level (SiOH + SiOH $\rightarrow$ SiOSi + H_2O). By iterating calculations after each reaction, they were able to reproduce the experimental evolution of α_{OH} as a function of the temperature. However, this method requires quantum chemistry calculations, which can be demanding from a computational perspective when performed on large systems. Recently, Fought et al.[36] proposed dehydroxylation strategies based on the silanol type, which is supported by Nuclear Magnetic Resonance (NMR) results. The following nomenclature is adopted to describe silanol types: *isolated*, *geminal* and *trio* silanols correspond to silicon atoms bonded to, respectively, one, two, and three hydroxyl groups, while two silanols sharing a common oxygen are called *vicinal* (Figure 4a).

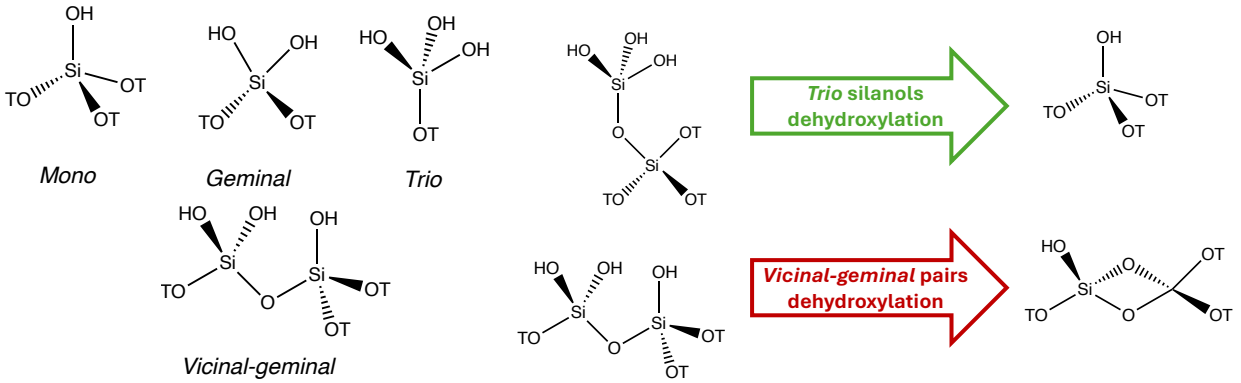

Figure 4: a) Classification of silanol groups, b) Silanol dehydroxylation scheme proposed by Fought et al. [36]

They assumed that trio silanols are very rare on the surface, so they are unlikely to be involved in catalytic processes. Therefore, the first step consists of deleting every trio silanols. This modification reduces α_{OH} from 7.9 to 7.2 OH nm^{-2}. Despite this improvement, there are still too many silanol groups. The second step focuses on vicinal silanols. Every vicinal pair containing a geminal silanol is condensed into a siloxane bridge (by losing one water molecule). The pairs of hydroxyl groups involved in the shortest hydrogen bond are deleted (Figure 4b). By applying this procedure, a slab with an α_{OH} of 5.0 OH nm^{-2} was produced, which corresponds to the targeted concentration (Table 4).

Table 4: Numbers and proportions of the isolated, geminal, and trio silanols at the surface of differently shaped amorphous silica frameworks and the impact of dehydroxylation strategies.

Slab	Isolated	%	Geminal	%	Trio	%	Total	α_{OH}(OH nm^{-2})
Hydrated	163	61.0	85	31.8	19	7.1	390	7.9
Without trio silanols	180	67.7	86	32.3	0	0.0	352	7.2
Without vicinal-geminal pairs	196	88.7	25	11.3	0	0.0	246	5.0
Tube								
Hydrated	412	64.9	191	30.1	32	5.0	890	7.2
Without trio silanols	440	68.5	202	31.5	0	0.0	844	6.8
Without vicinal-geminal pairs	457	91.0	45	9.0	0	0.0	547	4.4
MCM-41-like								
Hydrated	104	62.7	52	31.3	10	6.0	238	8.9
Without trio silanols	114	68.7	52	31.3	0	0.0	218	8.2
Without vicinal-geminal pairs	120	85.7	20	14.3	0	0.0	160	6.0

2.2.3 Defining the shape of the catalyst

One way to improve catalytic performances is to maximize the accessible surface, which is usually done by synthesizing porous materials because they display a large surface/volume ratio and an elevated specific surface area. [37] So, in this work, amorphous silica slabs serve as starting materials to model aluminosilicate catalysts. The protocol presented here to produce an amorphous silica structure is easily tunable to any catalyst shape. From a modeling perspective, creating a porous catalyst amounts to post-processing of the selected starting structure. Mesoporous silica constitutes a class of catalysts with pore size ranging from 20 Å to 500 Å. [38] Therefore, a mesoporous nanotube can be produced by carving a

hole in the amorphous silica framework generated via the melt-and-quench procedure. Modeling an infinite (along the z-axis) tube corresponds to deleting the atoms that do not satisfy the following equation.

$$R_{int} \leq \sqrt{(x_i - x_c)^2 + (y_i - y_c)^2} \leq R_{ext} \tag{8}$$

where x_i, y_i, and z_i are the coordinates of an atom i, x_c, y_c, and z_c are the coordinates of the center of the amorphous silica box, and R_{int} and R_{ext} are the radii determining respectively the pore size and the wall thickness (thickness = R_{ext} - R_{int}). On the other hand, some mesoporous silicates have a long-range organization, yielding more complex structures. Among the most widely used, MCM-41 [39] and SBA-15 [40] have a hexagonal porous architecture [38]. These materials can also be modeled from a crystal with similar symmetry as a starting point. So, among crystalline silica polymorphs, α-quartz has a hexagonal unit cell (a=b=4.916 Å, c=5.4505 Å, α=β=90° and, γ=120°). First, the melt-and-quench procedure was applied to a 8x8x2 α-quartz supercell. The mesoporous silicate with a hexagonal porous architecture was then created by deleting the atoms that do not satisfy Equation (8) at each corner of the periodic box (no need to specify R_{ext}). Both types of porous structures can then undergo the saturation/dehydroxylation procedure described in the previous section to produce realistic model catalysts with high surface area (Figure 5). Table 4 shows that the dehydroxylation scheme yields satisfactory α_{OH} for every structure.

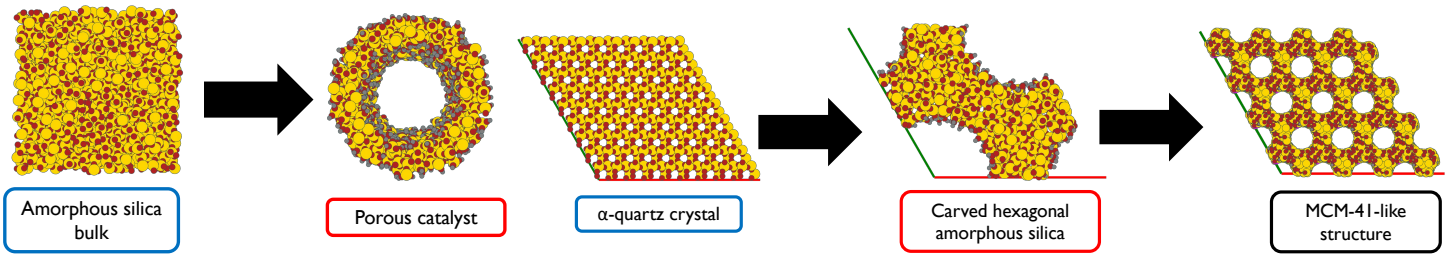

Figure 5: modeling of mesoporous silica a) Nanotube produced by carving holes in an amorphous silica box. b) Hexagonal porous architecture generated from an α-quartz supercell. The hexagonal pattern appears when the supercell is replicated.

2.3 Creation of clusters for QM calculations

This work aims at presenting a complete procedure to compute properties on amorphous silica-based catalysts. QM calculations are performed on small silica clusters extracted from an amorphous slab surface. This cluster approach relies on the assumption that, by exploring a sufficiently large number of configurations, the whole set of results should converge towards the average behavior of the studied material. [19] The general protocol is presented and tested for Brønsted amorphous aluminosilicate catalysts. Here, for each active site, hemispherical cuts are performed at the silica slab surface around targeted silicon atoms to generate the acid site models. The dangling bonds are then saturated using the algorithm presented in Section 2.2.1. The surface silicon atoms chosen as hemisphere centers must be bonded to four oxygen atoms themselves bonded to two silicon atoms (i.e., not involved in silanol groups). This condition is applied to represent Brønsted acid sites. The central silicon atom is then replaced by an aluminum atom and a proton is added on a neighboring oxygen atom as a balancing charge. These clusters are subjected to QM calculations.

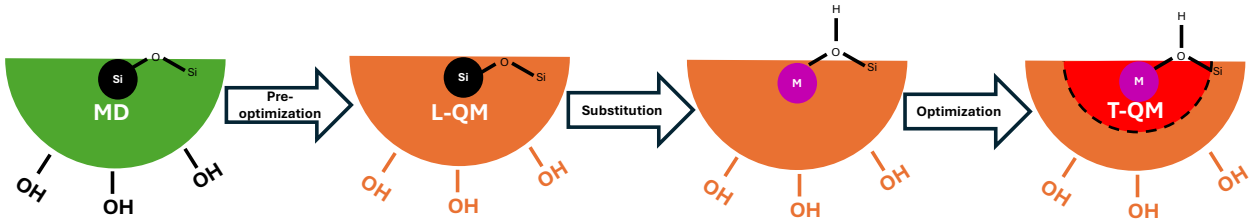

Figure 6: QM-Opt protocol to optimize the geometry of a silica cluster generated from MD (green), doped with a heteroelement (M=Al) adapted from Vandervelden et al.[29] A hemisphere is first extracted from an amorphous silica slab generated with MD. The cluster is saturated with O-H groups and "pre-optimized" at the DFT/QM level with a loose (L) convergence criterion (orange). The central atom is then replaced by the heteroelement (M) and a proton is added on a neighboring oxygen atom. The acid site is finally optimized with a tighter (T) convergence criterion (red), where only atoms close to the active site are allowed to move (delimited with dotted lines).

Vandervelden et al.[29] showed that in such a sequential MD-QM scheme, the properties computed can be biased by the initial MD structure. Therefore, they designed a multistep protocol to limit the influence of this so-called "procedural disorder". This scheme is adapted here. It starts with a geometry pre-optimization step, where the cluster structure is first fully relaxed at the DFT level. In this step, a "loose" convergence criterion is applied to reach an equilibrium geometry more quickly. Then, the acid site is created by substituting the central silicon atom with an aluminum atom and adding a hydrogen atom as a balancing charge on a neighboring oxygen atom. Those "doped" clusters are then "sliced" into tetrahedral atoms (Si or M) layers. The first layer corresponds to the aluminum atom and its neighboring oxygen atoms (including the one bearing the acidic proton), the second layer corresponds to the following silicon atoms and their neighboring oxygen atoms, and so on. This protocol ends with a second geometry optimization step, but here, the allowed geometrical relaxation cover at most the first four layers. Freezing terminal atoms allows to keep the constrained nature of the material. Here, a "tight" convergence criterion is applied to obtain the final structure (Figure 6).

2.4 QM Calculations parameters

These QM calculations are performed at the DFT level with the GAUSSIAN16[41] software. During the pre-optimization step, the B3LYP[42] XC functional and the 6-311G* basis set are used, the "loose" convergence criterion on RMS forces is 0.0017 au. The D3 dispersion corrections[43] were included in the last geometry optimization step, the "tight" convergence criterion on RMS forces is 0.00001 au. These optimized geometries were employed to calculate the harmonic vibrational frequencies and to simulate the IR absorption spectra. Those calculations used the same B3LYP-D3/6-311G* scheme. Magnetic shielding tensors were computed at the B3LYP/6-311G** level using the Gauge-Including Atomic Orbital (GIAO) scheme.

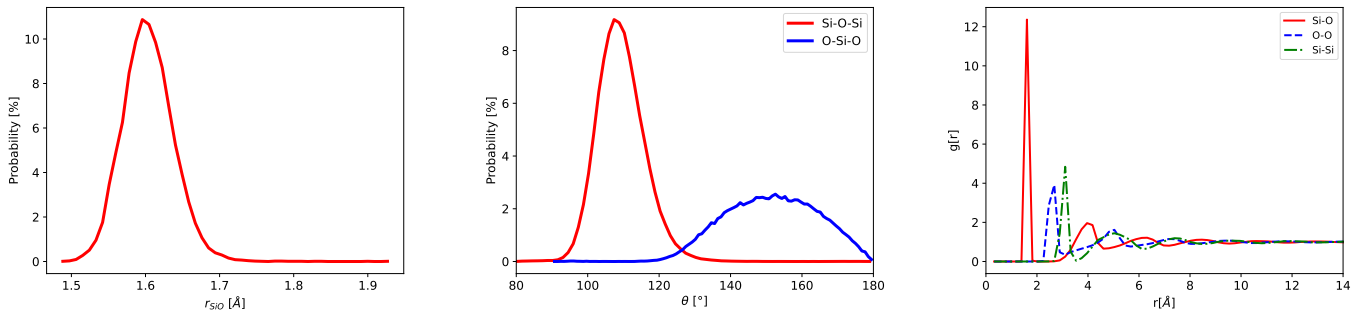

(a) (b) (c)

Figure 7: Structural analysis of amorphous silica frameworks produced by the melt-and-quench procedure from a β-cristobalite supercell: a) Si-O bond length distribution, b) Si-O-Si and O-Si-O angle distributions and c) Si-O, O-O, Si-Si RDFs.

3 Results and Discussion

3.1 MD-based melt-and-quench simulations

3.1.1 Basic structural analysis

The amorphous silica structure generated from the β-cristobalite is validated by the geometrical analysis shown in Figure 7. First, bond length and angle distributions are evaluated. The bond length distribution is centered at 1.60 ± 0.03 Å. This is close to 1.62 Å, which is the average Si-O bond length in amorphous silica frameworks as determined from X-ray diffraction (XRD).[44] The O-Si-O angle distribution (109.37 ± 6.68°) is narrower than for the Si-O-Si angle (151.46 ± 12.67°). The former represents the angle between the central Si atom and its four neighboring oxygen forming a tetrahedron. The latter angle distribution is wider and corresponds to the linkage between the tetrahedrons. The amorphous nature of such materials arise from the diversity of angles that link the tetrahedral silicon atoms. Bond and angle distributions allow to study the first neighboring shell of the atoms. By computing Radial Distribution Functions (RDFs), additional information can be gained on further atoms. RDFs describe the probability of finding an atom within a certain radius. The first Si-O peak ending at 1.9 Å represents the first neighboring shell (Figure 7c). The following peak is broader, confirming that the second neighboring shell is responsible for the disorder. Beyond the second layer, the curve flattens out, corresponding to an isotropic environment. This combination of short-range order and long-range disorder is characteristic of amorphous solids. O-O and Si-Si RDFs curves adopt similar shapes.
As mentioned above, by modifying the starting crystal during the procedure, catalysts of different shapes can be modeled. Therefore, α-quartz has been used to model a mesoporous catalyst with a hexagonal pore structure. As the protocol depicted here is intended to be general, the starting crystal should not influence the characteristics of the amorphous network produced by the melt-and-quench procedure. The same structural analysis has been adapted to validate the amorphous skeleton of a material generated from an α-quartz supercell (Figure S1). Indeed, the bond and angle distributions and RDFs were similar to those obtained when starting from β-cristobalite.

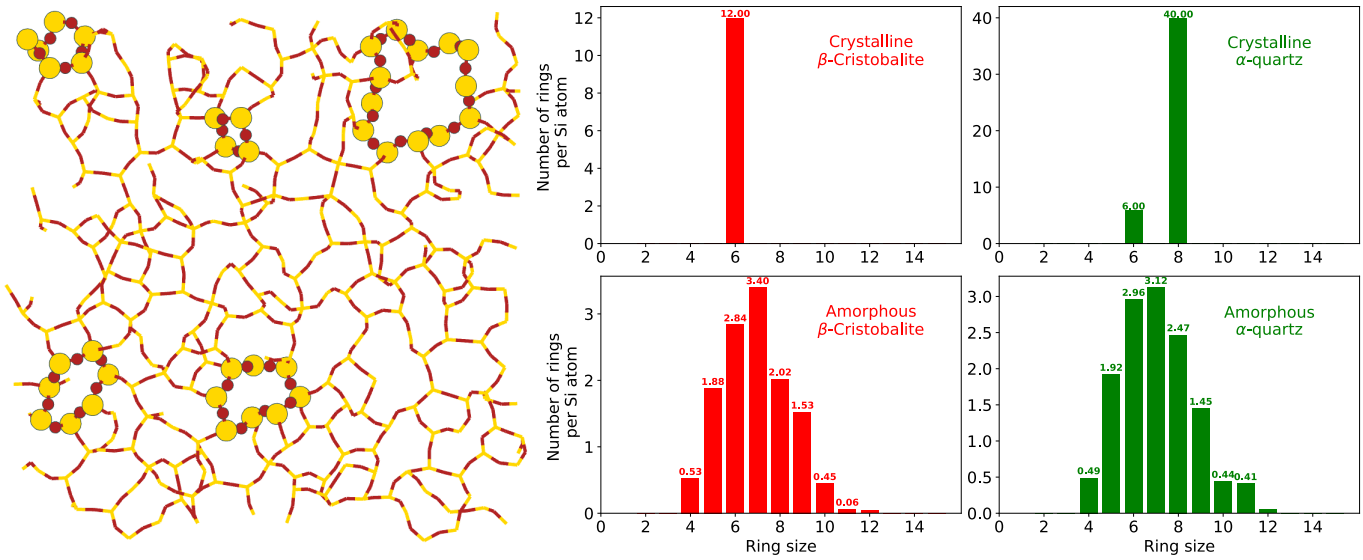

Figure 8: Selected primitive rings in an amorphous silica framework (left). Primitive rings distribution in amorphous silica frameworks produced by the melt-and-quench procedure and in their starting crystal unit cell (right).

3.1.2 Ring statistics

However, RDFs and angle distributions mostly describe the amorphous structure around the first two neighboring shells, which could be insufficient to identify remnants from the crystalline structure. These identifications can be done using ring statistics that reveal the medium-range disorder. Mysovsky and Paklin[45] used ring statistics to demonstrate that certain domains in the melted silica may retain structural similarities to the original crystal. Introduced in 1967,[46] ring statistics is an application of graph theory to describe materials. It is used to study the structure of zeolites or amorphous silica,[47,48] where the silicon and oxygen atoms correspond to the nodes and edges of the graph, respectively. In those topological networks, a path corresponds to a series of sequentially connected nodes, and a ring is a path that starts and ends at the same node. It is a useful tool to study amorphous systems beyond the second coordination sphere. There exist many classes of rings. In the context of this work, the focus is on primitive rings.[5] A primitive ring is defined as one that contains no shortcuts. Formally, it cannot be decomposed into two smaller rings.[49]

In an α-quartz unit cell each silicon atom contributes to forming six 6-membered primitive rings (6-rings) and 40 8-rings, while in the β-cristobalite unit cell, they are involved in the formation of 12 6-rings. On the contrary, a typical primitive ring analysis for amorphous silica yields a distribution centered around 7-rings.[50,51] Mysovsky and Paklin noticed that some amorphous silica frameworks generated via the melt-and-quench procedure from α-quartz were presenting an abnormally large number of 8-rings, demonstrating that the ring distribution should be assessed.[45] A primitive ring analysis has therefore been performed on α-quartz and β-cristobalite as well as on the amorphous silica frameworks generated from both crystalline structures (Figure 8). Searching for primitive rings in large structures is a computationally demanding task.[47] Yuan et al.[49] developed an efficient algorithm that can be decomposed into three steps. First, potential rings are searched by finding mid-nodes. A mid-node is the furthest node on the ring from a reference node. For any even 2n-ring, there is only one mid-node for each reference node. For any odd (2n+1)-ring, there are two mid-nodes for each check node, and they must be linked

Table 5: Primitive rings distribution of amorphous silica boxes generated via the melt-and-quench procedure. When the melting temperature is modified, the cooling rate is 5 K ps^{-1}. When the cooling rate is modified, the melting temperature is set to 5000 K.

	Ring size [n-rings]											
Temperature [K]	2	3	4	5	6	7	8	9	10	11	12	13
1000	0	0	0	0	12.00	0	0	0	0	0	0	0
2000	0	0	0	0	12.00	0	0	0	0	0	0	0
3000	0	0	0	0	12.00	0	0	0	0	0	0	0
4000	0	0	0	0.02	11.92	0.06	0	0	0	0	0	0
5000	0	0	0.53	1.88	2.84	3.40	2.02	1.53	0.45	0.06	0.04	0
6000	0	0	0.56	1.91	2.78	3.50	2.45	1.36	0.41	0.15	0.02	0
Cooling rate [K ps^{-1}]												
1	0	0	0.52	1.97	3.17	3.33	2.41	1.30	0.31	0.06	0.01	0
5	0	0	0.60	1.86	2.89	3.41	2.26	1.55	0.39	0.08	0.05	0
25	0	0	0.62	1.75	2.75	3.34	2.32	1.73	0.63	0.21	0.03	0.03
100	0	0	0.62	1.70	2.50	3.03	2.38	1.48	0.80	0.48	0.19	0.08

to each other. Then, rings are formed by joining all pairs of shortest paths (of length n) between the reference and mid-nodes. Finally, every ring that contains a shortcut is deleted, leaving all primitive rings. For this work, this algorithm has been implemented in an open source Python package.[52] After computations, β-cristobalite and α-quartz unit cells contain the expected amount of 6-rings and 8-rings. The primitive ring distributions of the amorphous silica framework generated from α-quartz and β-cristobalite are highly similar. There are very few 3 and 4-rings since they consist of strained positions. Most rings are between 5 and 8-rings, as already seen in the literature[51]. The absence of signatures corresponding to the initial crystals in the primitive ring distributions confirms that the melt-and-quench procedure does not depend on the starting structure.

3.1.3 Effect of melting temperature and cooling rate

The melting temperature of crystalline silica polymorphs stands around 1800 K.[53] However, most melt-and-quench procedures employ much higher temperatures.[23] This is usually justified by the need for total memory loss of the initial crystal structure. In this work, several melt-and-quench procedures were performed on β-cristobalite supercells with melting temperatures ranging from 1000 to 6000 K, while keeping the cooling rate constant (5 K ps^{-1}). RDF and primitive ring analysis have been used to study the influence of the melting temperature on the final amorphous structure. The primitive ring distribution analysis has proved to be a very powerful tool to detect traces of the original crystal structure (Table 5). Indeed, below 5000 K, almost all the rings formed are 6-membered, as in the β-cristobalite unit cell. Above 5000 K, the ring distribution becomes distributed around 7-rings, typical of amorphous silica frameworks. This can also be seen in the RDFs, which still exhibits some long-range organization (Figure S2). The same analysis has been performed with cooling rates ranging from 1 to 100 K ps^{-1}. In general, a very low cooling rate is recommended to give the atoms enough time to reorganize themselves and form an amorphous network. However, Table 5 and Figure S3 show that, for this range of cooling rates, no matter the cooling rate employed, a homogeneous distribution is always obtained.

3.2 QM cluster calculations

Once the amorphous nature of the generated catalyst has been established, the next step is to extract a cluster to calculate its properties. QM calculations require high accuracy within a reasonable computational time. In this section, several parameters of the QM-Opt protocol are varied to find the most cost-effective combination. On one hand, the cluster size and the region where the atomic positions are frozen, later referred as the "high layer", are modified. Indeed, the so-called partitioning scheme is crucial to take into account long-range interactions, but increasing the amount of atoms also increases the computational time. On the other hand, since DFT calculations are performed, the impact of the nature of the XC functional is also monitored, as the level of approximation has an impact on the calculation accuracy. Two quantities have been chosen to assess the validity of this sequential MD-then-QM approach, the DPE and ^{27}Al δ. The DPE is a widely computed metric to quantify the intrinsic strength of Brønsted acids.[12] It corresponds to the energy required to separate the proton of an acid from its conjugate base.

$$DPE = E_{A^-} + E_{H^+} - E_{HA} \tag{9}$$

where E_{A^-}, E_{H^+}, and E_{HA} are the energies of the deprotonated species, of the proton, and of the protonated species. Calculations were performed in gas phase (no solvent), therefore, the DFT energy of the proton is equal to zero. Both E_{HA} and E_{A^-} were obtained after geometry optimizations as described in Section 2.3.

The chemical shift is a descriptor of the chemical environment of an atom. It can be measured experimentally, so unlike DPE, the calculations can be directly compared with NMR data. It is calculated from the magnetic shielding tensor ($\boldsymbol{\sigma}$) corresponding to the magnetic field induced on an atom under the effect of an external magnetic field. The induced magnetic field results from the interaction of the atom electronic cloud with the external field. Thus, this quantity highly depends on the chemical environment of the targeted atom. The experimentally measured chemical shift is derived directly from the trace of $\boldsymbol{\sigma}$,[54]

$$\sigma_{iso} = \frac{1}{3} Tr\boldsymbol{\sigma} \tag{10}$$

σ_{iso} is the isotropic average of the magnetic shielding tensor, and

$$\delta = \sigma_{iso,ref} - \sigma_{iso,sample} \tag{11}$$

$\sigma_{iso,sample}$ and $\sigma_{iso,ref}$ are the isotropic averages of the magnetic shielding tensor of the studied atom in the sample and in a reference molecule. When studying ^{27}Al nuclei, $Al(H_2O)_6{}^{3+}$ is used as reference and $\sigma_{iso} = 577.74$ ppm.[55] For the ^{1}H nucleus, the reference is tetramethylsilane (TMS) with $\sigma_{iso} = 32.29$ ppm. These reference values were obtained from B3LYP/6-311G** calculations on B3LYP/6-311G* optimized geometries.

3.2.1 Study of the partitioning scheme

DPE and δ have been computed on a set of 24 acid sites to study the influence of the partitioning scheme on properties computed at the DFT level. The accurate description of the acid site surroundings is one of the main challenges of the cluster approach. Two parameters are considered, i) the size of the whole cluster and ii) the number of layers in the "high layer", i.e. where a high level method is employed. Hemispherical clusters of 7 Å, 9 Å, and 11 Å have been constructed. For each cluster, the "high layer" size has been enlarged up to four layers of tetrahedral atoms. The labeling scheme is simple: a 9 Å cluster with a two-layer large "high layer" is named C9L2.

The influence of the partitioning scheme on the DPE values and chemical shifts are summarized in Table S1. As illustrated in Figure 9, increasing both the cluster and the "high layer" sizes leads to lower DPE values. For the C11 series, no convergence towards a stable value is observed in the partitioning schemes investigated in this work. Similar behavior was observed by Trachta et al.[56] for DPE calculations on zeolite clusters of increasing sizes, even for clusters containing up to 150 tetrahedral atoms (twice as large as C11). This effect was justified by long-range electrostatic interactions. Apart from this, the standard deviations on the DPE (around 27 kJ mol^{-1}) remain very similar across all partitioning schemes, showing that the amorphous character of the clusters is well reproduced even with the smallest models. Due to the drift towards more negative values as a function of the system size, comparisons should be performed within fixed partitioning scheme. Those values fall in the typical 1200 kJ mol^{-1} range, which corresponds to what is obtained when computing DPE on aluminosilicate catalysts.[12,57]

The influence of the partitioning scheme is more systematic for the ^{27}Al chemical shifts as presented in Figure 9. For all cluster sizes, the average calculated δ values are about 75 ppm when only the central tetrahedron atom is included in the "high layer". Increasing the "high layer" size leads to smaller δ. For C9 and C11, the change gets less and less abrupt, reaching a plateau around 60 ppm. This can be understood as follows: only allowing the central tetrahedron to relax during the last step of the QM-Opt protocol (L1 case) does not allow the aluminum to adopt a fully stable position. Enlarging the relaxation zone allows reducing constraints on the positions of the atoms in the surroundings of the active site. Moreover, the standard deviation is also increasing with a larger "high layer". These calculated ^{27}Al chemical shifts are consistent with related calculations performed on tetrahedral Al atoms in silica frameworks.[58] Moreover, in solid-state NMR spectra, the signal corresponding to tetrahedral aluminum is usually observed as a broad peak centered around 60 ppm.[59] Indeed, the ^{27}Al atom possesses a nuclear quadrupole moment leading to interactions with the electric field gradient at the nucleus.[60] The magnitude of these quadrupolar interactions highly depends on the symmetry of the selected nucleus and on its close environment, so that the amorphous nature of materials yields a distribution of chemical shifts and of quadrupolar coupling constants, leading to this broadening. Subsequently, this leads to overlaps between signals corresponding to different Al species, which complicates the analysis of experimental spectra.[61] Note that these interactions also cause the broadening of the signal in crystalline aluminosilicates (such as zeolites). Therefore, we can conclude that a "high layer" larger than two tetrahedral layers (C9L3, C11L3, and C11L4) yields accurate δ values. Therefore, the C9L3 partitioning scheme appears to be a good compromise between accuracy and computational resources.

In the calculations reported so far, all clusters have been extracted from the same amorphous silica slab. Though our first purpose is to illustrate the calculation protocol, it is interesting to assess whether the

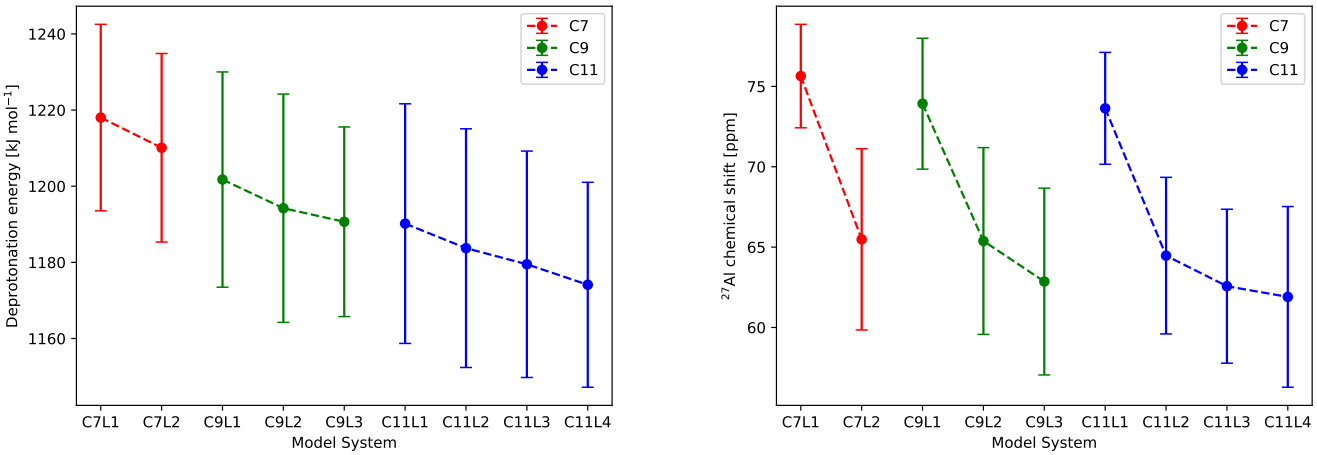

Figure 9: DPEs and ^{27}Al chemical shifts computed on hemi-spherical aluminosilicate clusters with different sizes and regions where atoms are allowed to relax during the QM-Opt protocol. Points represent the average values and error bars represent the standard deviations. The geometries were obtained at the B3LYP-D3/6-311G* level while the σ_{iso} values were computed at the B3LYP/6-311G** level.

configurational and chemical spaces are sufficiently explored. As a matter of fact, additional calculations were performed on three new sets of 10 aluminosilicate clusters. The first two were generated from MD simulations adopting the same melt-and-quench parameters as above (a melting temperature of 5000 K and a cooling rate of 5 K ps^{-1}), and the last one by using 6000 K as melting temperature (and the same cooling rate of 5 K ps^{-1}). All the other aspects of the calculations were kept the same. The results presented in Table S2 demonstrate overlaps between the different distributions as well as with the original one, though the number of clusters was kept low in these additional calculations. This demonstrates the reliability of the sampling of the configurational space.

3.2.2 Impact of the XC functional

While lots of studies have explored the design of suitable models (cluster vs periodic approaches), very few have focused on the effect of the XC functional.[19] Yet this parameter can be crucial for calculating properties when using DFT. In this section, DPE and chemical shifts have been computed on C9L3 clusters using 6 different XC functionals. Results obtained with two Generalized Gradient Approximation (GGA): BLYP[42,62], PBE[63], three hybrids: B3LYP[42], PBE0[64], M06-2X[40], and one range-separated hybrid ω-B97X-D[65] are compared in Figure 10 and Table S3. The QM-Opt protocol has been applied consistently with each XC functional. When computing DPE, dispersion corrections were included in the functional, with the exception of M06-2X since it has been designed to take into account these interactions. There is no systematic effect of the XC functional on the DPE values, i.e. for instance no systematic variation with the percentage of the Hartee-Fock (HF) exchange. Average DPE values range from 1170 to 1190 kJ mol^{-1}. As mentioned above, DPEs cannot be directly compared to experimental values. Yet, since the standard deviations are very similar for the different XC functionals there is no preferred XC functional.

The computed average chemical shifts fall within the 60-68 ppm range, which remains close to what is being experimentally measured (σ_{iso} value of ^{27}Al in $Al(H_2O)_6^{3+}$ computed with each XC functional can

be found in Table S4). Moreover, the difference in chemical shift between the different XC functionals can partly be attributed to the geometries obtained after the QM-Opt protocol. To show it, ^{27}Al chemical shifts have been computed with different XC functionals on the geometry obtained with B3LYP-D3. The red lines in Figure 10 effectively show that the differences between the XC functionals is slightly smaller than those of the black lines.

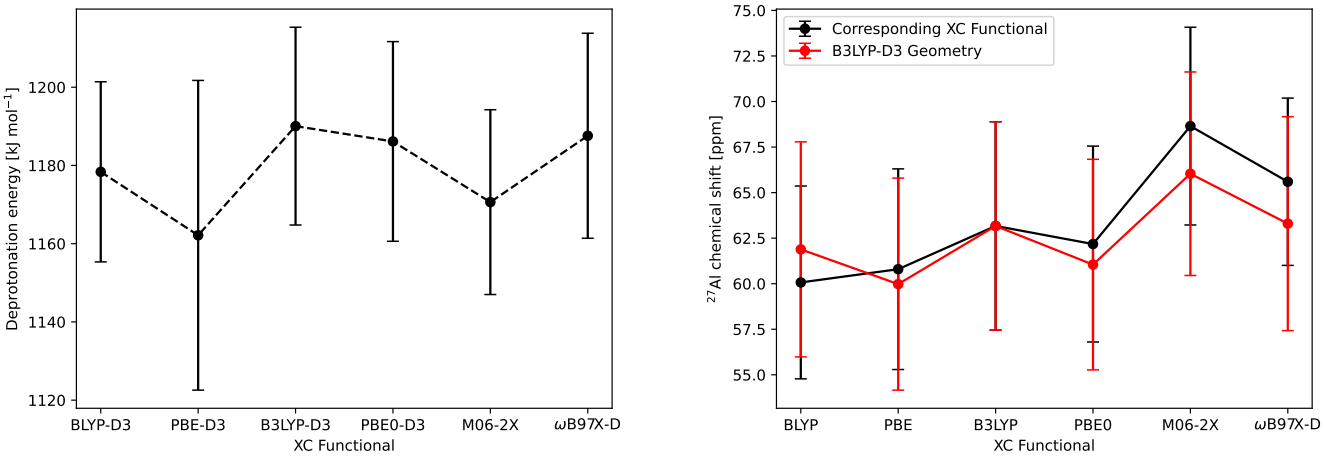

Figure 10: DPEs and ^{27}Al chemical shifts computed on the C9L3 hemi-spherical aluminosilicate cluster optimized with the QM-Opt protocol using different XC functionals. Points represent the average values and error bars represent the standard deviations. Geometries obtained with dispersion corrections except for M06-2X with the 6-311G* basis set and σ_{iso} obtained with the 6-311G** basis set.

3.2.3 modeling of other spectroscopic signatures

In addition to calculating the DPEs and ^{27}Al chemical shifts, the sequential MD-QM procedure has been enacted to determine two additional spectroscopic signatures of the bare aluminosilicate clusters bearing a Brønsted acid site, i.e. the IR spectrum in the O-H stretching region (3000 – 3800 cm^{-1}) and the ^{1}H NMR chemical shifts.[66,67] To do so, the optimized geometries of the 24 C9L3 clusters were employed. The harmonic vibrational frequencies were scaled by a 0.97 factor to account for anharmonicity contributions while a Gaussian broadening of 30 cm^{-1} was applied to each vertical transition. The IR spectrum of the amorphous aluminosilicate catalysts bearing a Brønsted acid function was then simulated by averaging out the contributions of the 24 C9L3 clusters (Figure 11). This simulated spectrum accurately reproduces the broad band ascribed to the silanol stretching frequency in this specific region. This large band accounts for all O-H stretching modes. Computing the vibrational frequencies allows to isolate the contribution arising from the stretching of the O-H group containing the acidic proton. These normal modes are mainly found in the 3600-3800 cm^{-1} region as observed for aluminosilicate materials.[66,68–71]. A good correlation was subsequently found between these silanol O-H vibrational frequencies and the corresponding equilibrium O-H bond lengths (Figure S4). Such observation has already been made within the IR spectrum analysis of an aluminated SBA-15 (a mesoporous aluminosilicate catalyst with amorphous structure) from periodic DFT calculations.[57]
Then, the ^{1}H chemical shifts were calculated using Equation (11). The signal corresponding to the acidic proton is observed between 3 and 11 ppm (4.96 ± 2.22 ppm), which is consistent with experimental spec-

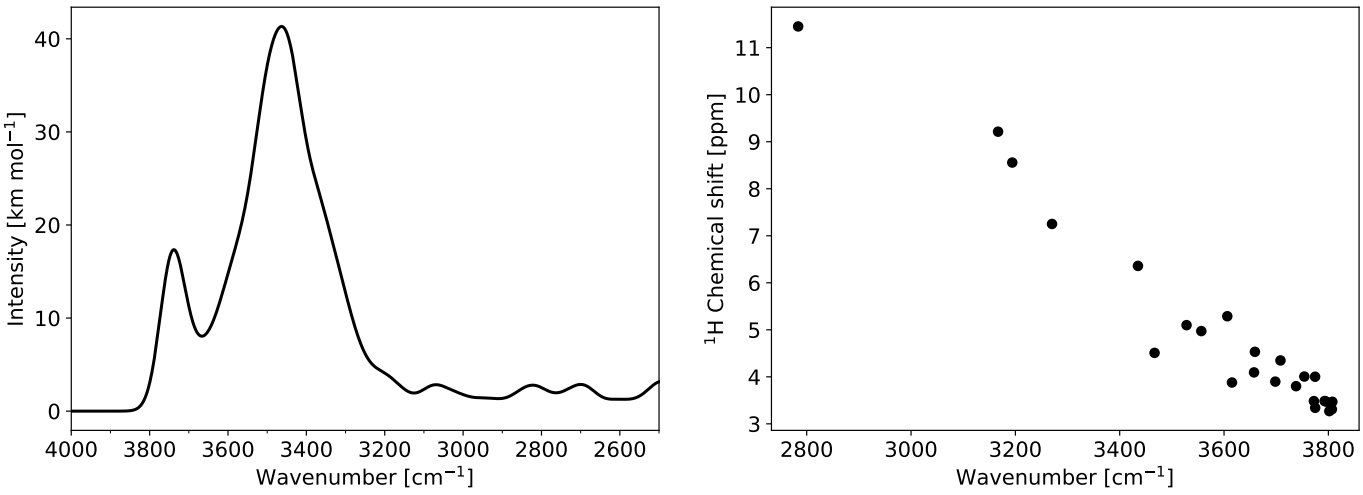

Figure 11: Simulated IR spectrum generated by averaging out the contributions of 24 amorphous aluminosilicate Brønsted C9L3 clusters. The harmonic vibrational frequencies were computed at the B3LYP-D3/6-311G* level. A scaling factor of 0.97 and a Gaussian broadening of 30 cm^{-1} have been applied at each vertical transition (left). Correlation between the acidic proton chemical shift and the O-H stretching vibrational frequency, only the O-H groups involving the acidic proton have been considered (right).

tra recorded on amorphous aluminosilicate materials.[72,73] Subsequently, a good correlation was revealed between these ^{1}H chemical shifts and the corresponding O-H stretching vibrational frequencies (Figure 11).

4 Conclusions and outlook

In this work, a complete route to compute chemical properties of amorphous aluminosilicate catalysts has been presented. Amorphous silica frameworks are generated via a melt-and-quench procedure using molecular dynamics simulation. Bond and angle distributions and RDFs are used to ensure the loss of long-range order from the initial β-cristobalite crystal. Using a homemade code, this analysis is completed by computing primitive rings distributions, which appears to be a powerful tool to analyze the impact of the melting temperature and of the cooling rate on the generated amorphous structure. This enables to establish that a melting temperature of 5000 K is necessary for obtaining an amorphous lattice, i.e. a lattice that no longer displays the ordered domains inherited from the initial crystal. Indeed, below a temperature of 5000 K, the 12 6-rings, typical of the β-cristobalite, are kept, while above this temperature, a wide distribution of ring sizes is obtained. Particular care has also been taken in the post-treatment of amorphous silica to model realistic catalysts. A hydration and dehydration procedure was undertaken to obtain a silanol concentration around 5 OH nm^{-2}, typical of what is observed experimentally. Next, catalysts with hexagonal porous architecture were modeled by manipulating an amorphous silica bulk.

In a second step, chemical properties are computed at the DFT level on hemispherical clusters carved from the saturated amorphous silica slabs. The geometries of the extracted clusters were optimized using a procedure similar to the QM-Opt protocol reported in the literature.[29] DPE and ^{27}Al chemical shift calculations were used to illustrate the influence of the partitioning scheme (the size of the whole cluster and of the atom relaxation zone) and of the XC functional on the calculated chemical proper-

ties. Regarding the partitioning scheme, a convergence towards chemical shifts values of 60 ppm is observed for a relaxation zone containing at least three layers of tetrahedral atoms (L3). Although DPE calculations did not give as clear a trend, the values obtained are around 1200 kJ mol^{-1}, similar to what can be found in the literature. Among the 6 tested XC functionals, no large differences are observed for these properties. In conclusion, performing QM calculations with a cluster approach on Brønsted amorphous aluminosilicate acid sites with a combination of the so-called C9L3 system with the B3LYP XC functional (using D3 dispersion corrections for geometry optimization) yields satisfactory DPE and ^{27}Al chemical shift values. Finally, those QM parameters have been used to compute other spectroscopic signatures, O-H stretching frequencies and ^{1}H chemical shifts, of the Brønsted acid sites.
The protocol depicted here is intended to be as general as possible. DPEs, chemical shifts, and vibrational frequencies have been computed, but this scheme can easily be extended to other properties (*e.g.* adsorption energy), and to other heteroelements (*e.g.* B, Ga, In), or acid sites (Lewis acid). Moreover, the proposed protocol could also be employed on surfaces with controlled roughness. These rough surfaces can be generated by following the method of Nguyen and Laird[74] by post-processing the selected starting structures. These rough structures are indeed of interest because they have a larger surface/volume ratio, influencing the catalyst performances.

Supporting Information
Supporting Information is available from the Wiley Online Library or from the author.

Acknowledgements
The authors thank the Wallonia-Brussels Federation for funding the "Action de Rcherche Concertée" (ARC) project entitled ACiDo-Catalysis (Convention No. 22/27-127, https://arc-projects.unamur.be/acdc). The calculations were performed on: (i) the computers of the Consortium des Équipements de Calcul Intensif (CÉCI, http://www.ceci-hpc.be) and particularly those of the Technological Platform of High-Performance Computing, for which the authors gratefully acknowledge the financial support of the F.R.S-FNRS, of the Walloon Region, and of the University of Namur (Conventions No. U.G006.15, U.G018.19, U.G011.22, RW1610468, RW/GEQ2016, RW2110213, and RW2210148), and (ii) on Lucia, the Tier-1 supercomputer of the Walloon Region, infrastructure funded by the Walloon Region (grant agreement No. RW1910247).

References

[1] R. Schlögl, *Angew. Chem. Int. Ed.* **2015**, *54* 3465.

[2] P. Gupta, S. Paul, *Catal. Today* **2014**, *236* 153.

[3] A. Taguchi, F. Schüth, *Microporous Mesoporous Mater.* **2005**, *77* 1.

[4] M. Shamzhy, M. Opanasenko, P. Concepción, A. Martínez, *Chem. Soc. Rev.* **2019**, *48* 1095.

[5] M. Shiga, A. Hirata, Y. Onodera, H. Masai, *Commun. Mater.* **2023**, *4* 91.

[6] A. Palčić, V. Valtchev, *Appl. Catal. A: Gen.* **2020**, *606* 117795.

[7] A. Vivian, L. Soumoy, L. Fusaro, P. Louette, A. Felten, S. Fiorilli, D. P. Debecker, C. Aprile, *J. Catal.* **2021**, *400* 83.

[8] A. Maertens, A. Vivian, L. Fusaro, A. Felten, P. Louette, M. Armandi, S. Fiorilli, C. Aprile, *Sustain. Energy Fuels* **2022**, *6* 3818.

[9] J. C. Bedoya, R. Valdez, L. Cota, M. A. Alvarez-Amparán, A. Olivas, *Catal. Today* **2022**, *388* 55.

[10] A. Maertens, C. Aprile, *Molecules* **2024**, *29* 102.

[11] M. Boronat, A. Corma, *ACS Catal.* **2019**, *9* 1539.

[12] P. Deshlahra, E. Iglesia, *Chem. Commun.* **2020**, *56* 7371.

[13] F. Zaera, *Catal. Lett.* **2012**, *142* 501.

[14] B. W. J. Chen, L. Xu, M. Mavrikakis, *Chem. Rev.* **2021**, *121* 1007.

[15] J. Sauer, *J. Catal.* **2024**, *433* 115482.

[16] E. A. Pidko, *ACS Catal.* **2017**, *7* 4230.

[17] P. Ugliengo, M. Sodupe, F. Musso, I. J. Bush, R. Orlando, R. Dovesi, *Adv. Mater.* **2008**, *20* 4579.

[18] F. Tielens, M. Gierada, J. Handzlik, M. Calatayud, *Catal. Today* **2020**, *354* 3.

[19] M. Caricato, *J. Phys. Chem. C* **2021**, *125* 27509.

[20] M. Groyne, B. Champagne, C. Baijot, M. D. Becker, *A & A* **2025**, *698* A284.

[21] J. M. Stallons, E. Iglesia, *Chem. Eng. Sci.* **2001**, *56* 4205.

[22] T. W. Dijkstra, R. Duchateau, R. A. van Santen, A. Meetsma, G. P. A. Yap, *J. Am. Chem. Soc.* **2002**, *124* 9856.

[23] K. Vollmayr, W. Kob, K. Binder, *Phys. Rev. B* **1996**, *54* 15808.

[24] J. Geske, M. Vogel, *Mol. Simul.* **2017**, *43* 13.

[25] R. T. Cygan, J. A. Greathouse, A. G. Kalinichev, *J. Phys. Chem. C* **2021**, *125* 17573.

[26] B. W. H. van Beest, G. J. Kramer, R. A. van Santen, *Phys. Rev. Lett.* **1990**, *64* 1955.

[27] S. Halbert, S. Ispas, C. Raynaud, O. Eisenstein, *New J. Chem.* **2018**, *42* 1356.

[28] P. N. Wimalasiri, N. P. Nguyen, H. S. Senanayake, B. B. Laird, W. H. Thompson, *J. Phys. Chem. C* **2021**, *125* 23418.

[29] C. Vandervelden, A. Jystad, B. Peters, M. Caricato, *Ind. Eng. Chem. Res.* **2021**, *60* 12834.

[30] R. T. Cygan, J.-J. Liang, A. G. Kalinichev, *J. Phys. Chem. B* **2004**, *108* 1255.

[31] J. C. Phillips, D. J. Hardy, J. D. C. Maia, J. E. Stone, J. V. Ribeiro, R. C. Bernardi, R. Buch, G. Fiorin, J. Hénin, W. Jiang, R. McGreevy, M. C. R. Melo, B. K. Radak, R. D. Skeel, A. Singharoy, Y. Wang, B. Roux, A. Aksimentiev, Z. Luthey-Schulten, L. V. Kalé, K. Schulten, C. Chipot, E. Tajkhorshid, *J. Chem. Phys.* **2020**, *153* 044130.

[32] C. D. Williams, K. P. Travis, N. A. Burton, J. H. Harding, *Microporous Mesoporous Mater.* **2016**, *228* 215.

[33] J.-P. Gallas, J.-M. Goupil, A. Vimont, J.-C. Lavalley, B. Gil, J.-P. Gilson, O. Miserque, *Langmuir* **2009**, *25* 5825.

[34] F. Tielens, C. Gervais, J. F. Lambert, F. Mauri, D. Costa, *Chem. Mat.* **2008**, *20* 3336.

[35] C. S. Ewing, S. Bhavsar, G. Veser, J. J. McCarthy, J. K. Johnson, *Langmuir* **2014**, *30* 5133.

[36] E. L. Fought, Y. Han, T. L. Windus, I. I. Slowing, T. Kobayashi, J. W. Evans, *Microporous Mesoporous Mater.* **2022**, *341* 112077.

[37] P. Sudarsanam, E. Peeters, E. V. Makshina, V. I. Parvulescu, B. F. Sels, *Chem. Soc. Rev.* **2019**, *48* 2366.

[38] J. Liang, Z. Liang, R. Zou, Y. Zhao, *Adv. Mater.* **2017**, *29* 1701139.

[39] C. T. Kresge, M. E. Leonowicz, W. J. Roth, J. C. Vartuli, J. S. Beck, *Nature* **1992**, *359* 710.

[40] D. Zhao, J. Feng, Q. Huo, N. Melosh, G. H. Fredrickson, B. F. Chmelka, G. D. Stucky, *Science* **1998**, *279* 548.

[41] M. J. Frisch, G. W. Trucks, H. B. Schlegel, G. E. Scuseria, M. A. Robb, J. R. Cheeseman, G. Scalmani, V. Barone, G. A. Petersson, H. Nakatsuji, X. Li, M. Caricato, A. V. Marenich, J. Bloino, B. G. Janesko, R. Gomperts, B. Mennucci, H. P. Hratchian, J. V. Ortiz, A. F. Izmaylov, J. L. Sonnenberg, Williams, F. Ding, F. Lipparini, F. Egidi, J. Goings, B. Peng, A. Petrone, T. Henderson, D. Ranasinghe, V. G. Zakrzewski, J. Gao, N. Rega, G. Zheng, W. Liang, M. Hada, M. Ehara, K. Toyota, R. Fukuda, J. Hasegawa, M. Ishida, T. Nakajima, Y. Honda, O. Kitao, H. Nakai, T. Vreven, K. Throssell, J. A. Montgomery Jr., J. E. Peralta, F. Ogliaro, M. J. Bearpark, J. J. Heyd, E. N. Brothers, K. N. Kudin, V. N. Staroverov, T. A. Keith, R. Kobayashi, J. Normand, K. Raghavachari, A. P. Rendell, J. C. Burant, S. S. Iyengar, J. Tomasi, M. Cossi, J. M. Millam, M. Klene, C. Adamo, R. Cammi, J. W. Ochterski, R. L. Martin, K. Morokuma, O. Farkas, J. B. Foresman, D. J. Fox, Gaussian 16 Rev. C.01, **2016**.

[42] A. D. Becke, *J. Chem. Phys.* **1993**, *98* 5648.

[43] S. Grimme, *Wiley Interdiscip. Rev. Comput. Mol. Sci.* **2011**, *1* 211.

[44] R. L. Mozzi, B. E. Warren, *J. Appl. Crystallogr.* **1969**, *2* 164.

[45] A. S. Mysovsky, A. S. Paklin, *Glass Phys. Chem.* **2023**, *49* 269.

[46] S. V. King, *Nature* **1967**, *213* 1112.

[47] S. Le Roux, P. Jund, *Comput. Mater. Sci.* **2010**, *49* 70.

[48] J. T. Crum, J. R. Crum, C. Taylor, W. F. Schneider, *Microporous Mesoporous Mater.* **2023**, *351* 112466.

[49] X. Yuan, A. N. Cormack, *Comput. Mater. Sci.* **2002**, *24* 343.

[50] L. W. Hobbs, C. E. Jesurum, V. Pulim, B. Berger, *Philos. Mag. A* **1998**, *78* 679.

[51] Q. Zhou, Y. Shi, B. Deng, J. Neuefeind, M. Bauchy, *Sci. Adv.* **2021**, *7* eabh1761.

[52] Crubirig, Crubirig/ring_search, **2025**.

[53] W. Pabst, E. Gregorova, *Ceram. - Silik.* **2013**, *57* 167.

[54] J. C. Facelli, *Prog. Nucl. Magn. Reson. Spectrosc.* **2011**, *58* 176.

[55] R. W. Schurko, R. E. Wasylishen, A. D. Phillips, *J. Magn. Reson.* **1998**, *133* 388.

[56] M. Trachta, R. Bulánek, O. Bludský, M. Rubeš, *Sci. Rep.* **2022**, *12* 7301.

[57] S. Perez-Beltran, P. B. Balbuena, G. E. Ramírez-Caballero, *J. Phys. Chem. C* **2016**, *120* 18105.

[58] T. Ohkubo, A. Masuno, E. Tsuchida, S. Ohki, *J. Phys. Chem. C* **2024**, *128* 1298.

[59] M. Zheng, Y. Chu, Q. Wang, Y. Wang, J. Xu, F. Deng, *Prog. Nucl. Magn. Reson. Spectrosc.* **2024**, *140* 1.

[60] A. P. M. Kentgens, *Geoderma* **1997**, *80* 271.

[61] K. Chen, Z. Gan, S. Horstmeier, J. L. White, *J. Am. Chem. Soc.* **2021**, *143* 6669.

[62] C. Lee, W. Yang, R. G. Parr, *Phys. Rev. B* **1988**, *37* 785.

[63] J. P. Perdew, K. Burke, M. Ernzerhof, *Phys. Rev. Lett.* **1996**, *77* 3865.

[64] C. Adamo, V. Barone, *J. Chem. Phys.* **1999**, *110* 6158.

[65] J.-D. Chai, M. Head-Gordon, *Phys. Chem. Chem. Phys.* **2008**, *10* 6615.

[66] C. Schroeder, V. Siozios, M. Hunger, M. R. Hansen, H. Koller, *J. Phys. Chem. C* **2020**, *124* 23380.

[67] L. Treps, C. Demaret, D. Wisser, B. Harbuzaru, A. Méthivier, E. Guillon, D. V. Benedis, A. Gomez, T. de Bruin, M. Rivallan, L. Catita, A. Lesage, C. Chizallet, *J. Phys. Chem. C* **2021**, *125* 2163.

[68] G. Crépeau, V. Montouillout, A. Vimont, L. Mariey, T. Cseri, F. Maugé, *J. Phys. Chem. B* **2006**, *110* 15172.

[69] K. Góra-Marek, J. Datka, *Appl. Catal. A: Gen.* **2006**, *302* 104.

[70] F. Leydier, C. Chizallet, A. Chaumonnot, M. Digne, E. Soyer, A.-A. Quoineaud, D. Costa, P. Raybaud, *J. Catal.* **2011**, *284* 215.

[71] A. J. J. Koekkoek, J. A. R. van Veen, P. B. Gerrtisen, P. Giltay, P. C. M. M. Magusin, E. J. M. Hensen, *Microporous and Mesoporous Mater.* **2012**, *151* 34.

[72] G. I. Yucelen, R. P. Choudhury, J. Leisen, S. Nair, H. W. Beckham, *J. Phys. Chem. C* **2012**, *116* 17149.

[73] Z. Wang, K. Chen, Y. Jiang, J. Trébosc, W. Yang, J.-P. Amoureux, I. Hung, Z. Gan, A. Baiker, O. Lafon, J. Huang, *J. Phys. Chem. Lett.* **2021**, *12* 11563.

[74] N. P. Nguyen, B. B. Laird, *J. Phys. Chem. A* **2023**, *127* 9831.

Table of Contents

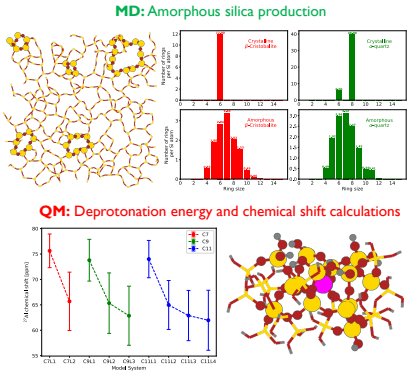

A cluster approach: Chemical properties of Brønsted aluminosilicate catalysts are computed using a sequential MD-then-QM approach. The amorphous silica slabs are generated from MD and analyzed through their primitive rings distributions. DFT calculations are then performed on hemispherical clusters extracted from the silica slabs.